Georg-August-Universität Göttingen

Acoustic Resonances in High Lift Configuration

S. Hein, T. Hohage, W. Koch and J. Schöberl

Preprint Nr. 2006-16

Preprint-Serie des
Instituts für Numerische und Angewandte Mathematik
Lotzestr. 16-18
D - 37083 Göttingen

Acoustic Resonances in a High Lift Configuration

By STEFAN HEIN[1], THORSTEN HOHAGE[2] WERNER KOCH[1] AND JOACHIM SCHÖBERL[3]

[1]Institute of Aerodynamics and Flow Technology, DLR Göttingen, Germany

[2]Institute for Numerical and Applied Mathematics, University of Göttingen, Germany

[3]Centre for Computational Engineering Science, RWTH Aachen University, Germany

(Received 29 June 2006)

Low- and high-frequency acoustic resonances are computed numerically via a high-order finite element code for a two-dimensional, two-element high lift configuration with a leading edge slat. Zero mean flow is assumed approximating the low Mach number situation at aircraft landing and approach. To avoid unphysical reflections at the truncated domain boundaries perfectly matched layer absorbing boundary conditions are implemented in the form of the complex scaling method of atomic and molecular physics. It is shown that two types of resonances exist: resonances of surface waves which scale with the total airfoil length and longitudinal cavity-type resonances which scale with the slat cove length. The latter depend strongly on the slat cove geometry and determine the peaks in the frequency spectrum. All resonances are damped due to radiation losses but can be excited by self-excited shear layers if the shear-layer frequency is close to a resonant frequency resulting in increased tonal noise.

1. Introduction

Through technological progress, such as ultra high bypass ratio turbofan engines and improved acoustical liners in the nacelle, aircraft engines of modern commercial airliners have become significantly more quiet in the past four decades. With the efficient reduction of engine noise airframe noise has emerged as an ever more important component of the overall aircraft noise especially during aircraft approach and landing when the engines are at low power, cf. Crighton (1991). Experimental studies on both sides of the Atlantic based on free flight tests of production aircraft, cf. Michel *et al.* (1998) (various aircraft), Piet *et al.* (2002) (Airbus A340), Stoker *et al.* (2003) (Boeing 777), or wind tunnel tests of scaled aircraft models, cf. for example Grosche *et al.* (1997) (Airbus A340), Hayes *et al.* (1997) (DC 10), Davy *et al.* (2002) (Airbus A320/A321), Soderman *et al.* (2002) (Bombardier CRJ-700), Oerlemans & Sijtsma (2004) (Airbus A340), Horne *et al.* (2005) (Boeing 777), pinpointed high lift devices and landing gears as dominant sources of airframe noise. In order to better understand the noise source mechanisms and find ways to reduce the noise emission various aircraft components were investigated in more detail by advanced experimental and computational tools. In addition to broadband noise strong tones were observed under certain operating conditions in many of the above experiments. These tones were traced amongst others to the region around the leading-edge slat and trailing-edge flap of the high lift configuration, cf. Dobrzynski *et al.* (1998) (ALVAST high lift model), Khorrami *et al.* (2000) (high lift model), Olson

et al. (2000) (high lift model), Dobrzynski *et al.* (2001) (Airbus A320 full scale wing) or Dobrzynski & Pott-Pollenske (2001) (high lift model).

The above mentioned strong tones are highly undesirable because they cause a significant increase in perceived noise level. The occurrence of low- and high-frequency tones under different operating conditions (for example different slat deflections) suggest the presence of different source mechanisms generating the low- and high-frequency tones. Using unsteady Reynolds averaged Navier–Stokes (URANS) simulations with a high spatial resolution Khorrami *et al.* (2000) were able to prove their conjecture that self-excited vortex shedding at the blunt trailing edge of the slat is the likely source for the tonal peak in the acoustic spectra at high frequencies: for a 30^o slat deflection they observed vortex shedding from the slat trailing edge, the frequency of which was in close agreement with the tonal frequency measured in a corresponding experiment conducted at NASA Langley Research Center. Simulations at 20^o slat deflection showed no vortex shedding which agreed with no tonal noise emission in the NASA Langley experiment. The vortex shedding at the trailing edge of the slat has since been confirmed by experimental investigations of Olson *et al.* (2000) and Takeda *et al.* (2002). Singer *et al.* (2000) used the URANS data of Khorrami *et al.* (2000) to compute the acoustic far field by an acoustic analogy formulation based on the Ffowcs Williams-Hawkins equation.

In their paper Khorrami *et al.* (2000) raised the question as to whether a feedback mechanism is operative in the gap between the slat and the main wing. This so-called gap resonance was investigated by Tam & Pastouchenko (2001) and Agarwal & Morris (2002) using a simple wall jet model. They conjectured that the shedding frequency at the slat trailing edge might be regulated by an acoustic feedback loop: when the shedding frequency matches one of the transverse resonance frequencies of the gap between the slat and the main wing, an intense tone is produced. Based on this feedback loop Tam & Pastouchenko (2001) developed a simple formula for the gap tone frequency as a function of gap height, local flow speed and the local speed of sound. For a finite length plate above a semi-infinite wall Hein *et al.* (2004) showed that for zero flow the one-dimensional gap resonances of Tam & Pastouchenko (2001) agree exactly with the least damped two-dimensional resonances. The gap resonances are resonances of transverse modes corresponding to the dominating modes in a simple two-mirror laser cavity. However, the slat cove resembles more a shallow open cavity than a laser cavity, and in a shallow cavity the longitudinal modes dominate, cf. Koch (2005). Probably this is the reason why the frequencies computed via the simple acoustic feedback formula of Tam & Pastouchenko (2001) differed markedly from the experimental results of Takeda *et al.* (2002). Takeda *et al.* (2004) extended the wall jet model of Tam & Pastouchenko (2001) to include the slat cove region using an idealised two-dimensional slat model. Performing a systematic variation of slat overlap and gap their compressible URANS computations indeed indicated a strong influence of the slat/wing geometry on the high-frequency tones.

Contrary to the source mechanism of the high-frequency tones various source mechanisms have been proposed for the low-frequency tones, cf. Guo (1997); Olson *et al.* (2001); Pott-Pollenske *et al.* (2003), albeit cavity shear tones within the slat cove are the most likely source of the low-frequency tones as conjectured by Roger & Pèrennés (2000) and Takeda *et al.* (2001). After the trailing-edge noise studies Khorrami *et al.* (2002) extended their URANS plus far-field computations to the free shear layer originating at the slat cusp to investigate the low-frequency noise source. The fully turbulent simulations of Khorrami *et al.* (2002) proved overly diffusive and required explicit forcing of the shear layer to excite and maintain the large-scale structures. To circumvent the excessive diffusive effects of the turbulence model they used an ad hoc zonal approach in

later versions, cf. Khorrami *et al.* (2004). With this the shear layer became self-excited and large-scale coherent structures, vortex merging and ejection of vortices through the slat gap were observed and compared quite well with the accompaning experimental studies of Jenkins *et al.* (2004). Qualitatively similar flow structures were found in the experiments of Takeda *et al.* (2001) or Kaepernick *et al.* (2005) who investigated a swept wing model. In their most recent paper Choudhari & Khorrami (2006) accounted for the three-dimensionality of flow fluctuations and found considerable improvement in the accuracy of the unsteady near-field solution. The eventual goal of their computational simulations is a physics based prediction of the broadband slat noise sources.

The objective of the present paper is the computation of low- and high-frequency acoustic resonances (also termed scattering frequencies) for a generic two-element high lift system with a leading-edge slat. No account is taken of the underlying noise generation mechanisms of these tones and mean flow effects are neglected assuming that the resonances depend only weakly on Mach number. However, it should be clearly pointed out that the noise sources in the form of shear layers exist only if mean flow is present. Hein *et al.* (2004) argued that acoustic resonances in the high lift system could provide a viable mechanism for the selection of a particular frequency: if the resonances are near any source frequency and are only weakly damped one can expect high noise levels and enhanced airframe noise which should be discernible in unsteady CFD simulations. Hein *et al.* (2005) computed the low-frequency resonances of a generic three-element high lift configuration without flow and the computed resonances turned out to be very close to the low-frequency tonal frequencies measured by Pott-Pollenske *et al.* (2003). Surprisingly the resonant frequencies were practically independent of the slat cove geometry. This meant that the low-frequency resonances cannot be resonances of the slat cove but are resonances of surface waves. In the literature such surface waves are called Franz-type creeping waves, cf. Überall *et al.* (1977), which resonate when exactly n wavelengths fit over the circumference of the whole high lift configuration. In Hein *et al.* (2005) we proved the surface wave assertion by numerically computing the resonances of a circular cylinder without flow and compared the computed resonances with analytic results of Morse & Ingard (1968) for the corresponding diffraction problem.

On the other hand the slat cove acts like a shallow cavity and the corresponding resonances should scale with the length of the slat cove between slat hook and main wing. To test this hypothesis we investigated first the resonances of an extended model problem, namely a circular cylinder with a rectangular cutout, finding that the cavity resonances dominate at high frequencies. Similarly, the slat cove resonances dominate at higher frequencies albeit not as distinctly as for the model problem due to the more complicated geometry and the cavity being open between slat and main wing which causes higher damping. But even weakly damped resonances can be excited by self-excited shear layers and these resonances determine the lobes in the far-field radiation pattern.

The outline of the paper is as follows. After a brief summary of the solution method in Section 2 the different physical character of surface wave resonances and cavity resonances is demonstrated for the simple model problem of a circular cylinder with a rectangular cutout in Section 3. In Section 4 acoustic resonances are computed for a generic two-element high lift configuration with a leading-edge slat only. The influence of slat cove parameters on the resonances is investigated in Section 5 and a short conclusion completes the paper.

2. Governing Equation and PML Boundary Condition

The equation governing acoustic disturbances in a medium with zero mean flow is the wave equation. Due to the large spanwise extent of the slat system the high lift configuration can be treated as two-dimensional. In the following all lengths will be nondimensionalised with a characteristic reference length l^*_{ref}, velocities with the ambient speed of sound c^*_0, densities with the ambient density ρ^*_0, and pressures with $\rho^*_0 c^{*2}_0$. Here the asterisk superscript denotes a dimensional quantity. Assuming periodic time dependence $\exp(-i\omega^* t^*)$, where ω^* is the circular frequency, the wave equation can be reduced to the Helmholtz equation

$$\Delta\phi(x,y) + K^2\phi(x,y) = 0 \tag{2.1}$$

for the (nondimensional) velocity potential $\phi(x,y)$. $\Delta = \partial^2/\partial x^2 + \partial^2/\partial y^2$ is the two-dimensional Laplacian in (nondimensional) Cartesian coordinates x, y and $K = \omega^* l^*_{ref}/c^*_0$ denotes the dimensionless frequency, with $K/2\pi$ being the Helmholtz number, cf. Helmholtz (1954). The time-independent dimensionless disturbance velocity and pressure are then given by $\mathbf{v}(x,y) = \nabla\phi$ and $p(x,y) = iK\phi$, respectively. In addition to the Neumann boundary condition $\partial\phi/\partial n = 0$ on solid walls a radiation condition has to be imposed at infinity. For scattering problems with real $K > 0$ the standard radiation condition due to Sommerfeld is

$$\lim_{r\to\infty} r^{1/2}\left(\frac{\partial\phi}{\partial r} - iK\phi\right) = 0, \tag{2.2}$$

which has to be satisfied uniformly in all directions. In the following we shall consider (2.1) as an eigenvalue equation, and the eigenvalues K^2 will correspond to *complex* frequencies K with $\mathrm{Im}(K) < 0$. In this case Sommerfeld's radiation condition is no longer a valid characterisation of outgoing waves. Alternative formulations of the radiation condition also valid for $\mathrm{Im}(K) < 0$ include complex coordinate stretching (or complex rescaling) studied in Reed & Simon (1978), the pole condition suggested by Frank Schmidt as discussed in Hohage *et al.* (2003*a*), Hohage *et al.* (2003*b*), series representations, and integral representations.

Numerical computations are necessarily conducted on truncated domains. Without nonreflecting or absorbing boundary conditions at the finite grid boundaries, which approximate the radiation condition at infinity, unphysical reflections at the latter often cause large errors. After Bérenger (1994) introduced his perfectly matched layer (PML) absorbing boundary condition it quickly became the method of choice in computational electrodynamics as well as acoustics, see for example the recent review by Hu (2004). Modelling a physically absorbing layer in Cartesian coordinates Bérenger (1994) added fictitious damping terms in his split-field Maxwell equations with the remarkable property that no reflections are generated at the interface for all frequencies and angles of wave incidence. It was soon recognised that Bérenger's PML formulation is equivalent to a complex coordinate stretching, cf. Chew & Weedon (1994), which can be interpreted as an analytic continuation of the governing equations into a complex spatial domain, see Chew *et al.* (1997); Collino & Monk (1998); Lassas & Somersalo (1998). This can easily be implemented into existing finite difference or finite element codes, and PML formulations in 3D Cartesian, cylindrical or spherical coordinates soon became available. For example, in polar coordinates one introduces instead of r the complex variable

$$\rho(r,\omega) = r + \frac{i}{\omega}\sigma(r). \tag{2.3}$$

The damping function $\sigma(r)$ is usually expressed in power form, cf. Hu (2004), smoothly

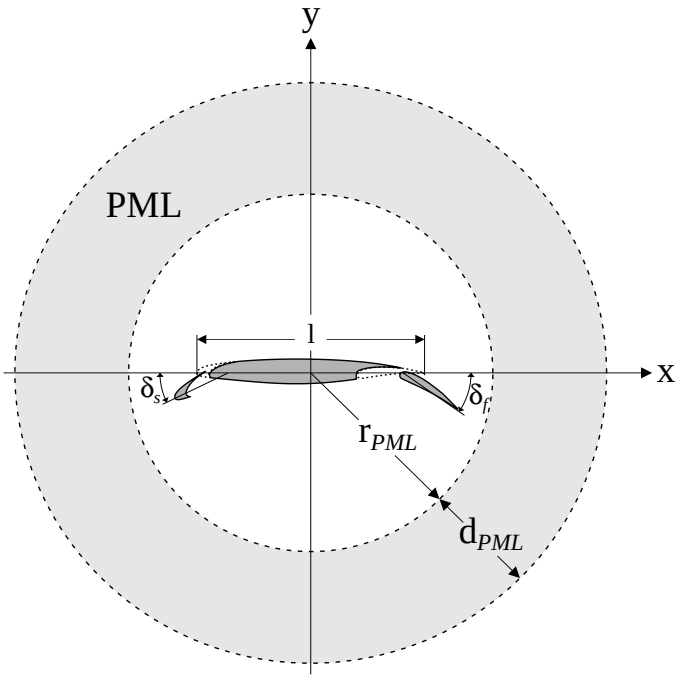

FIGURE 1. Generic three-element high lift configuration of Pott-Pollenske *et al.* (2003) at landing approach with annular PML.

starting at the PML interface $r = r_{PML}$, e.g.

$$\sigma(r) = \begin{cases} \sigma_0 \, (r - r_{PML})^{\beta}, & r > r_{PML} \\ 0, & r \leq r_{PML}. \end{cases} \tag{2.4}$$

For a positive (real) damping coefficient $\sigma_0 > 0$ and constant $\beta \geq 1$ outgoing waves will decay exponentially in the PML. In numerical computations the PML can therefore be truncated at $r_{PML} + d_{PML}$ as shown schematically in figure 1 for a typical high lift configuration with a leading-edge slat with deflection δ_s and a trailing-edge flap with deflection δ_f. Here d_{PML} denotes the width of the PML, and instead of enforcing (2.2) a Dirichlet boundary condition can be imposed at the outer edge of the PML, cf. Collino & Monk (1998). The error due to artificial reflections at this truncated outer edge of the PML is small if σ_0 and d_{PML} are chosen properly.

For scattering problems ω is a prescribed (real) constant and therefore can be absorbed into the damping coefficient σ_0. Then the above PML formulation is practically identical with the *complex scaling method* of atomic and molecular physics, cf. the recent survey by Moiseyev (1998) or the monograph by Hislop & Sigal (1996). For resonance problems ω is part of the solution and the PML formulation (2.3) would result in a nonlinear eigenvalue problem with much larger coefficient matrices when solving the problem numerically. Consequently, for the numerical computation of resonances in unbounded space it is advantageous to use the complex scaling method, i.e. (2.3) without ω, see for example Hein *et al.* (2004). Then the damping coefficient is no longer constant but has to be adjusted to the relevant frequency domain.

As mentioned before, the above PML formulation can be easily implemented into existing finite element codes. For the present paper we use the high-order finite element code NGSolve of Joachim Schöberl. Before proceeding with the computation of resonances in

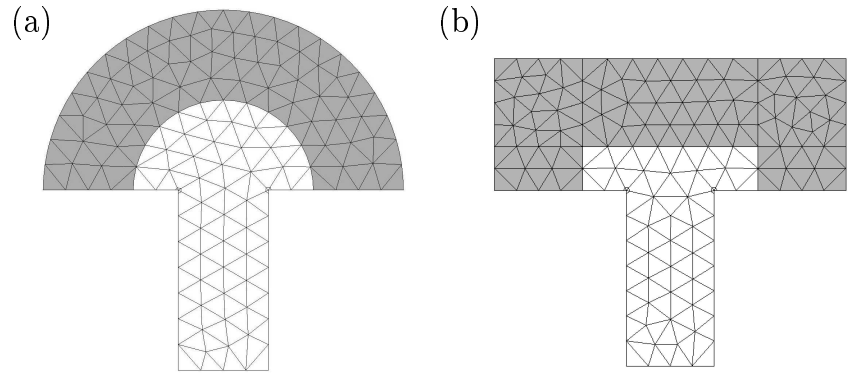

FIGURE 2. Finite element grids for $l/d = 0.5$ cavity with $\Delta = 0.3$. (a) annular PML with $r_{PML} = 1$ and $d_{PML} = 1$, (b) rectangular PML with $x_{PML} = \pm 1$, $y_{PML} = 0.5$ and $d_{PML} = 1$.

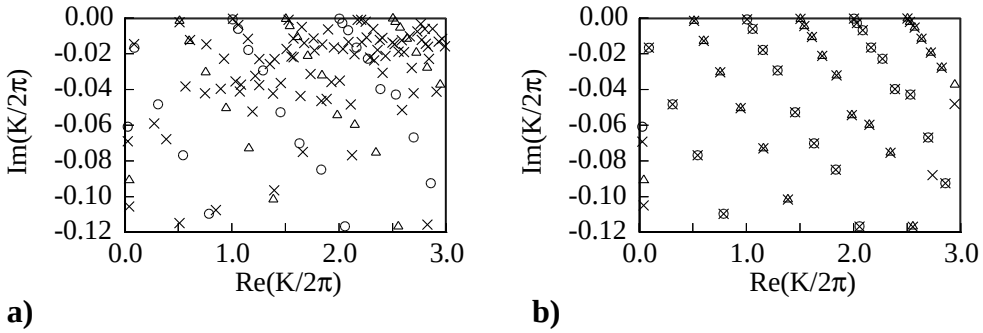

FIGURE 3. Comparison of resonances in two-dimensional rectangular cavity with $l/d = 0.5$ obtained via spectral collocation method of Koch (2005)($\circ$ symmetric, $\triangle$ antisymmetric in x) and via finite element method ($\times$) using mesh of figure 2a with PML parameters $\sigma_0 = 5$, $\beta = 1$, but differing FE polynomial order p: (a) $p = 2$ ($N_{dof} = 721$), (b) $p = 12$ ($N_{dof} = 9217$).

open domains with more complicated boundaries we validated our finite element code by comparing the results for a two-dimensional rectangular open cavity $l/d = 0.5$ with the resonances computed by Koch (2005) which were verified with the classical semi-analytic results of Tam (1976). For this example we chose the reference length l^*_{ref} to be the cavity length l^* such that $l = 1$. $d = 2$ is then the depth of the cavity for our chosen test example. For $y \geq 0$ we apply an annular PML with $r_{PML} = 1$ and $d_{PML} = 1$ and generate a triangulated macro mesh with maximum mesh size $\Delta = 0.3$ using the net generating code NETGEN of Schöberl (1997), cf. figure 2a. Near the singular exit corners of the cavity the grid was refined locally. The computed resonant frequencies are depicted in figure 3. The open symbols correspond to the results computed by Koch (2005) via the multi-domain spectral collocation method and the cross symbols represent our present results obtained for the mesh of figure 2a via the finite element code NGSolve. This comparison constitutes a severe test for both computations: in the collocation method a strong formulation with C^1 continuity across the rectangular domain boundaries is employed in conjunction with a rectangular PML, and the eigenvalue problem is solved by a standard EVP solver. The variational formulation of the finite element code requires only C^0 continuity across the triangular mesh elements and utilises an annular PML together with a shifted Arnoldi algorithm. Keeping the same mesh, i.e. $\Delta = 0.3$, we vary the order p of the FE polynomial on a triangular element, and hence the number

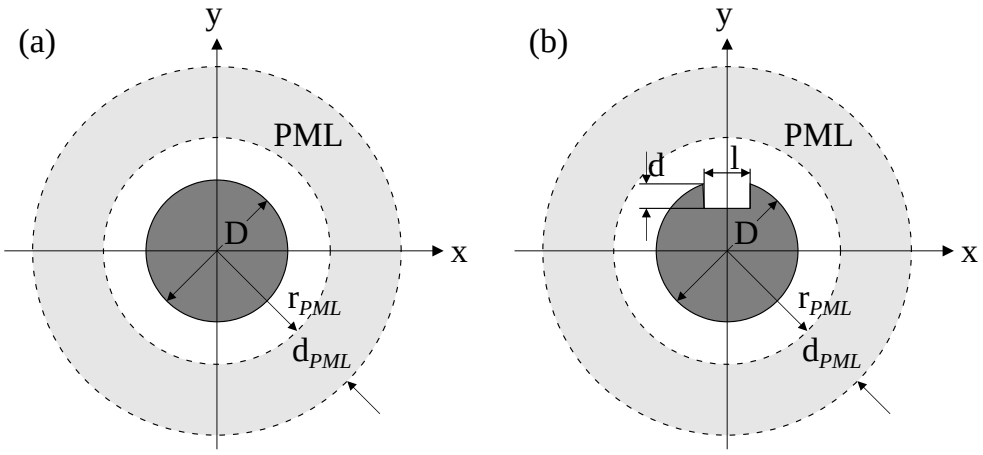

FIGURE 4. (a) Solid circular cylinder and (b) circular cylinder with a two-dimensional rectangular cavity enclosed by annular PML.

of degrees of freedom N_{dof}. Figure 3a shows the spectrum using $p = 2$ while figure 3b shows the resonant frequencies for $p = 12$. It is quite apparent that for the coarse mesh of figure 2a a high order finite element code is a necessity. Practically identical results were obtained using the rectangular PML shown in figure 2b.

3. Resonances for a cylinder with a rectangular cutout

After validating our finite element code NGSolve we investigated the resonances of a simple model problem namely a rigid circular cylinder with a rectangular cavity carved out on one side of the cylinder as depicted in figure 4b. This way we hope to get a deeper insight into the physics behind the resonances of a high lift configuration. For this model problem the natural choice for the reference length l^*_{ref} is the diameter D^* of the cylinder, i.e. $K_D = \omega^* D^*/c_0^*$. Without the cavity, cf. figure 4a, only resonances of surface waves are possible as demonstrated by Hein *et al.* (2005). By introducing a rectangular cavity of depth d and length l, which we use to model a slat cove, cavity resonances are added which modify these surface wave resonances. Varying the parameters l/D and l/d the cavity resonances can be changed in a wide range while the surface wave resonances remain almost constant. For our results, shown in figure 5 and discussed in the following, we chose $l/D = 1/6$ and $l/d = 2$.

The complex resonances of the surface waves computed for the solid cylinder of figure 4a are depicted by the solid dots in figure 5a. The classical solution for the pressure $p_s(r, \varphi)$ of an acoustic wave scattered by an infinite rigid cylinder of radius $R = D/2$ can be written down explicitly, cf. Morse & Ingard (1968) p.400ff,

$$p_s(r,\varphi) = -\hat{p}_i \sum_{n=0}^{\infty} (2 - \delta_{n0})\, i^n \frac{J_n'(kR)}{H_n^{(1)'}(kR)} H_n^{(1)}(kr)\, \cos(n\varphi). \tag{3.1}$$

Here φ is measured from the direction of the incoming plane wave with amplitude $\hat{p}_i$ and propagating in x direction, δ_{n0} is Kronecker's delta, $k = \omega^*/c_0^*$ is the wavenumber, J_n is the n^{th} order Bessel function and $H_n^{(1)}$ is the n^{th} order Hankel function of the first kind. Complex resonances (also called scattering frequencies) occur at the zeros of $H_n^{(1)'}(z) = 0$ (so-called n^{th} Franz zero) which can be computed easily via Newton – Raphson iteration. The first ten zeros ($n = 1, \ldots, 10$) computed this way are marked by

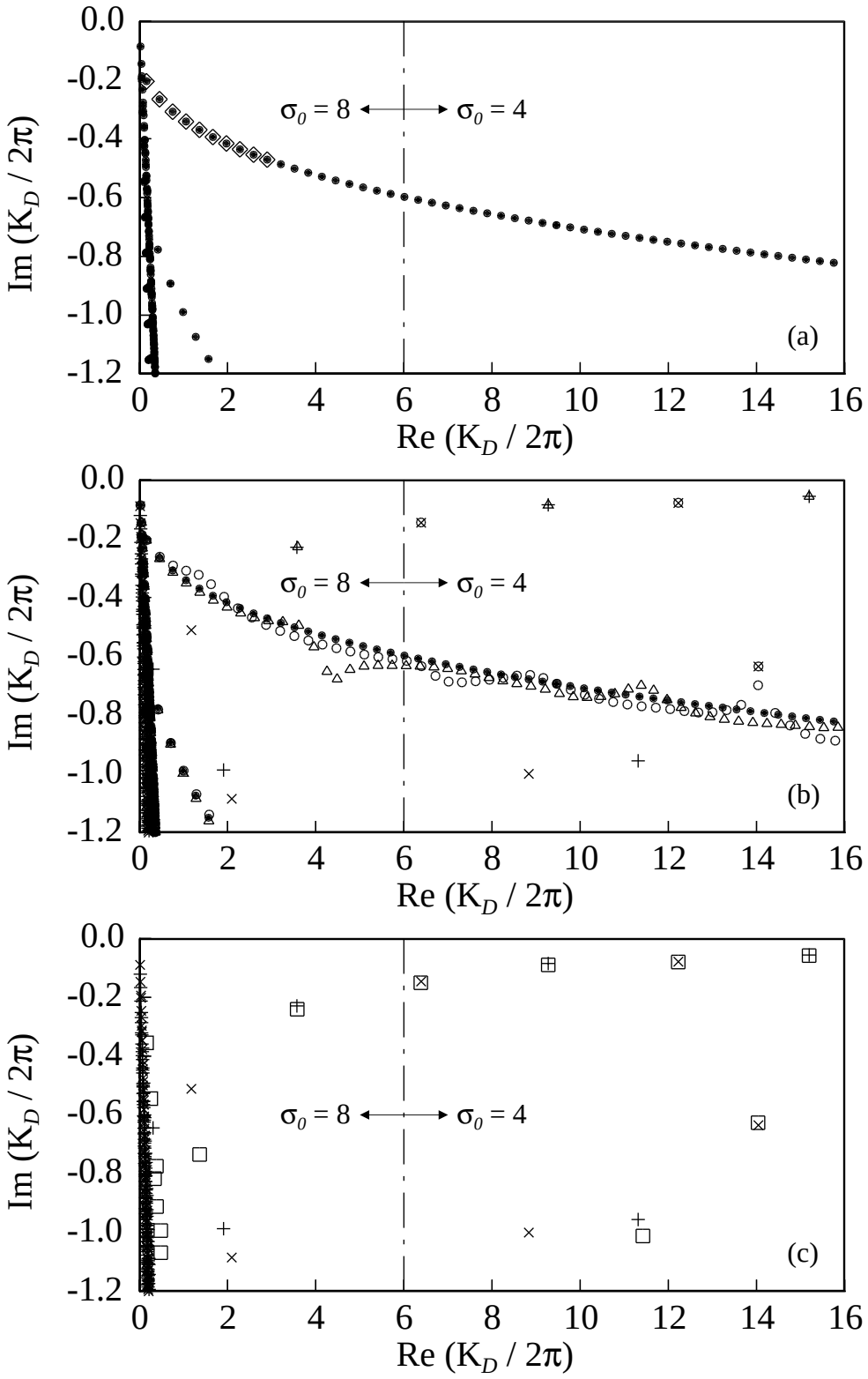

FIGURE 5. (a) Surface wave resonances for a solid circular cylinder: • numerical resonances, ◇ first ten zeros of $H_n^{(1)'}(z) = 0$ in (3.1). (b) Resonances for a circular cylinder with a two-dimensional rectangular cavity with $l/D = 1/6$, $l/d = 2$: ∘, △ symmetric and antisymmetric resonances, • surface wave resonances replotted from figure 5a, ×, + symmetric and antisymmetric cavity resonances replotted from figure 5c. (c) Cavity resonances for $l/D = 1/6$, $l/d = 2$: ×, + symmetric and antisymmetric resonances for cavity on cylinder, □ resonances of Koch (2005) for cavity in half plane.

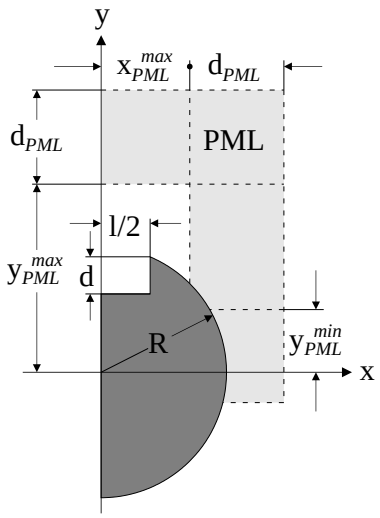

FIGURE 6. Circular cylinder with a two-dimensional rectangular cavity enclosed by rectangular PML.

the diamond symbols in figure 5a and agree very well with our numerically computed resonances. In our numerical computation we considered only the half cylinder for $x \geq 0$ with Dirichlet or Neumann conditions imposed at the plane $x = 0$. Due to symmetry the resonances for the Dirichlet and Neumann problem are equal, i.e. the plotted resonances are double resonances.

In electromagnetic scattering theory the frequency region when the dimensions of the scattering object are comparable to the wavelength is called resonance region, and the frequently used canonical model of a perfectly conducting circular cylinder is very similar to our above acoustical model. For this model Heyman & Felsen (1983) demonstrated the connection between creeping waves and complex resonances. In particular they showed that the complex resonances can be identified by two indices (m, n), where n marks the angular harmonics and m is associated with the creeping waves. In figure 5a mainly the $m = 1$ branch is shown with the first ten zeros $n = 1, \ldots, 10$ marked by the diamond symbols, whereas the resonances of the $m = 2$ branch are highly damped and therefore not so important in our acoustical problem.

If the rectangular cavity is added to the cylinder, as sketched in figure 4b, the double resonances of figure 5a split into symmetric and antisymmetric surface wave resonances as depicted by the open circles and triangles respectively in figure 5b. The weakly damped symmetric and antisymmetric resonances correspond to cavity resonances. To demonstrate this more clearly we surrounded the cavity with a rectangular PML, as sketched in figure 6, and computed the corresponding resonances. This way surface wave resonances are excluded. Again imposing Neumann or Dirichlet conditions at the symmetry plane $x = 0$ we obtained the symmetric and antisymmetric cavity resonances marked by the cross and plus symbols respectively in figure 5c. For comparison we replotted the resonances of Koch (2005) for a rectangular cavity in a half plane in figure 5c by the open square symbols. Again the longitudinal resonances are the least damped resonances for this shallow cavity with $l/d = 2$ and of the longitudinal cavity resonances only the fundamental resonance shows a noticeable influence of the cylinder curvature.

In figure 5 the dash-dotted lines indicate where we patched together two overlapping spectra computed with different PML and Arnoldi shift parameters, i.e. $\sigma_0 = 8$ for

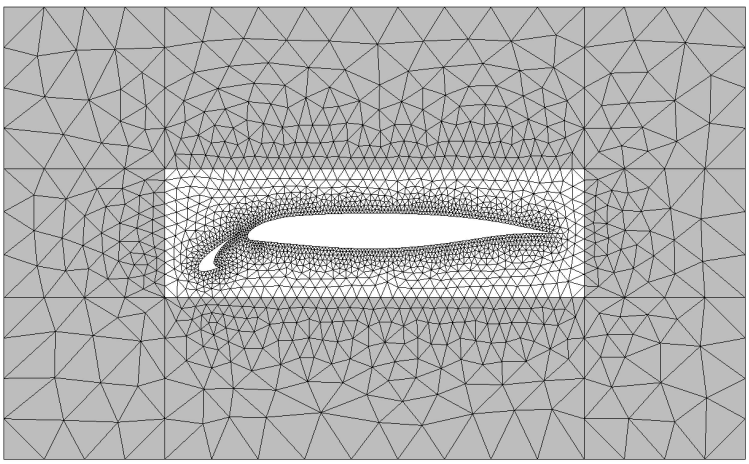

FIGURE 7. Finite element grid of two-element high lift configuration with slat angle $\delta_s = 26^o$, slat overlap $o_s = 0.018$, slat gap $g_s = 0.0217$ and rectangular PML (shaded region).

$Re(K_D/2\pi) < 6$, and $\sigma_0 = 4$ for $Re(K_D/2\pi) \geq 6$. For the annular PML we used $r_{PML} = 0.7$ and for the rectangular PML of figure 6 we chose $x_{PML}^{max} = 0.3$, $y_{PML}^{max} = 0.7$. In both cases the PML thickness was $d_{PML} = 0.5$. The order p of the FE polynomial was taken to be $p = 10$, and the maximal mesh size Δ in the above computations was $\Delta = 0.1$. The resonances near the negative imaginary axis are the discrete approximations of the continuous spectrum and should be disregarded for our present investigation.

From figure 5b we conclude that the resonances of a circular cylinder with a two-dimensional shallow rectangular cavity consist of two types: resonances of the surface waves and longitudinal cavity resonances with the longitudinal cavity resonances being the least damped resonances. A sequence of resonances with imaginary part tending to 0 has to be expected since there exist trapped rays between the side walls of the rectangular cavity. This was conjectured early by Lax & Phillips (1967). For a review of rigorous results on the distribution of resonances we refer to Zworski (1999).

4. Resonances for an airfoil with leading-edge slat

With the insight gained from the model problem we proceed now with the computation of the acoustic resonances of a two-element high lift configuration consisting of the main airfoil and a leading-edge slat as depicted in figure 7 corresponding to the three-element geometry investigated experimentally by Pott-Pollenske *et al.* (2003) with a retracted flap. For our baseline configuration we chose a slat angle $\delta_s = 26^o$, a slat overlap $o = -0.018$ and a slat gap $g = 0.0217$ (see figure 14 for the definition of the slat parameters). Now the reference length l^*_{ref} is taken to be the chord length l^* of the clean wing with the slat stowed (cruise condition), cf. figure 1. Then $K = \omega^* l^*/c_0^*$ and figure 7 shows a typical grid with maximal mesh size $\Delta = 0.1$. To keep the degrees of freedom as low as possible in our finite element computation we used a rectangular PML and refined the grid locally in the slat cove and around the two airfoils.

Following the approach taken for our model problem we solve the high lift configuration first with a retracted slat in order to obtain the surface wave resonances of the high lift configuration in cruise condition. To avoid the weakly damped whistling tones from the gap between the retracted slat and the main wing, as observed in figure 6 of Hein *et al.* (2005), we eliminate this gap by smoothing the contour (in experiments this is often

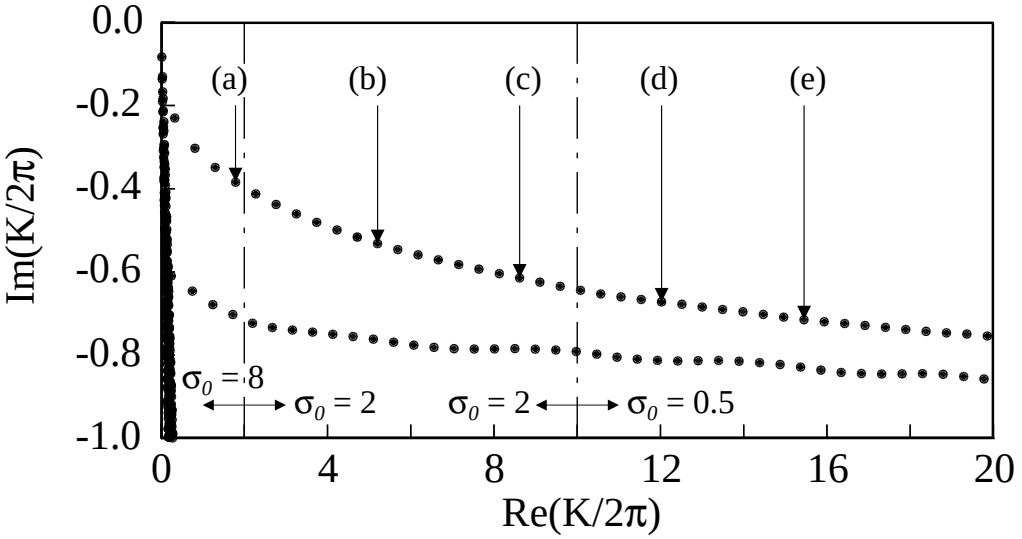

FIGURE 8. Surface wave resonances (•) for high lift configuration with retracted slat (clean wing) and rectangular PML: $d_{PML} = 0.5$, $\Delta = 0.1$, $p = 12$. The overlapping spectra are patched together at the dash-dotted lines.

done with clay). The corresponding surface wave resonances are depicted in figure 8 up to $Re(K/2\pi = 20)$. For this we patched together the spectrum from three overlapping spectra with different σ_0 (and Arnoldi shifts) as indicated in figure 8. In our finite element computation we used the polynomial order $p = 12$. Without the symmetry of our model problem the double resonances of the circular cylinder in figure 5a split into two distinct branches starting with a dipole-like eigenfunction similar to the one shown by Hein *et al.* (2005) for the symmetric NACA0012 profile. A few of the higher surface wave eigenfunctions corresponding to the resonances marked (a) to (e) in figure 8 are depicted in figure 9.

Next, we compute the resonances in the slat cove of our baseline configuration with extracted slat and slat angle $\delta_s = 26^o$ excluding all surface wave resonances around the whole wing. This can be achieved by surrounding the extracted slat by an annular PML ending on the main wing as shown in figure 10 where a corresponding grid is depicted. The resulting least damped resonances are shown in figure 11 together with three sample eigenfunctions. Note that for these slat parameters the least damped resonances are not the gap modes of Tam & Pastouchenko (2001) but modes which resemble longitudinal cavity modes, cf. Koch (2005), with n nodal lines between slat hook and main wing.

Finally, we consider the high lift baseline configuration with the slat extracted at a slat angle of $\delta_s = 26^o$ as depicted in figure 7. Contrary to the clear separation of surface wave resonances and cavity resonances in our model problem now the slat cove resonances interact strongly with the surface wave resonances and we obtain the spectrum depicted in figure 12. Again we patched together the spectrum from three overlapping spectra with different σ_0 as indicated in figure 12 by the dash-dotted lines. The resonances are depicted by open circles. Also included are the surface wave resonances for the clean wing of figure 8 by solid dot symbols and the slat cove resonances of figure 11 by the star symbols. In general the resonances of the high lift configuration with extracted slat have much lower radiation losses than the clean configuration, i.e. more noise is radiated to the far field. Only for very low frequencies do the resonances follow the surface wave resonances which are essentially independent of slat cove geometry. For a three-element

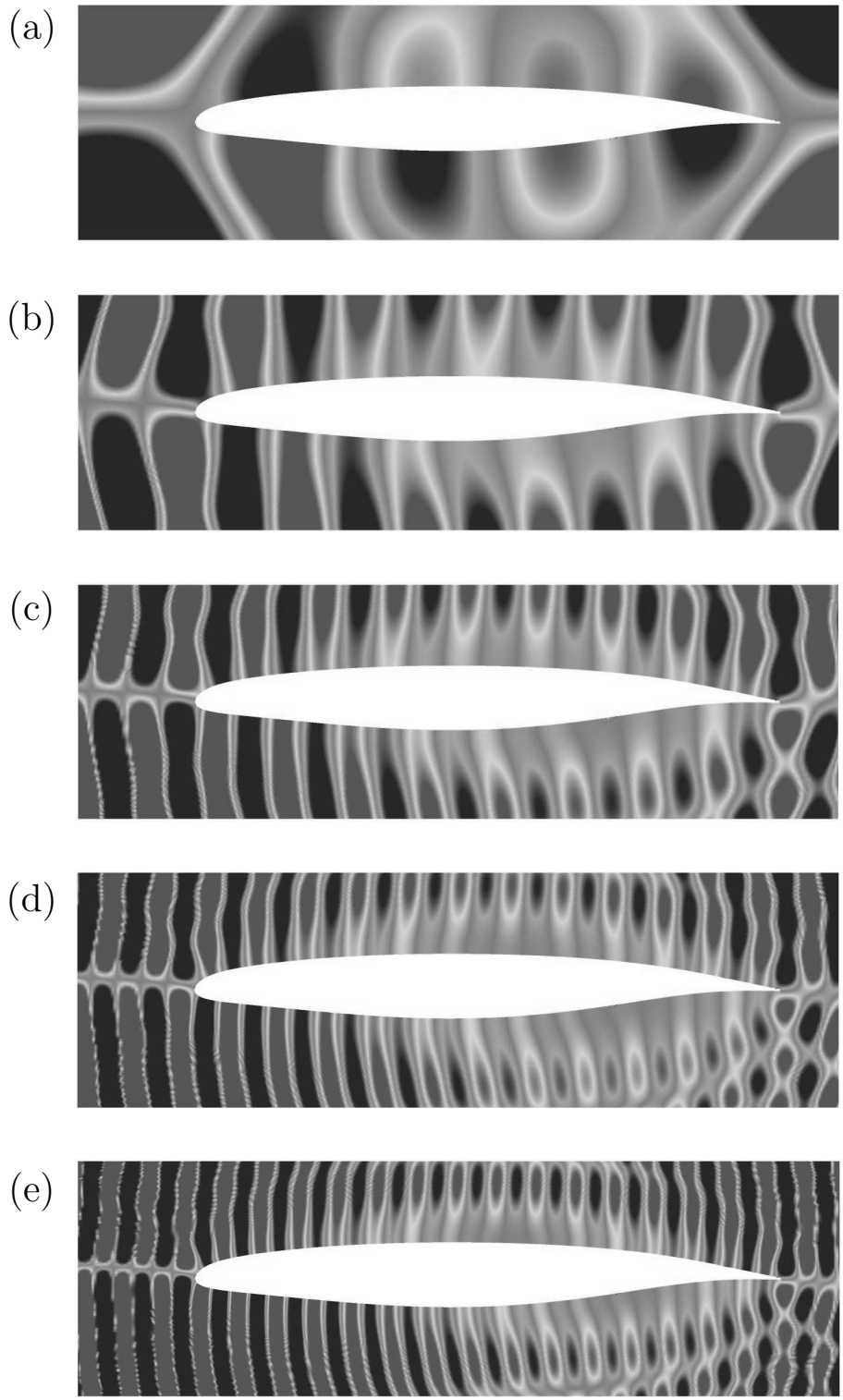

FIGURE 9. Clean wing eigenfunctions $(a), \ldots, (e)$ corresponding to the five surface wave resonances marked in figure 8.

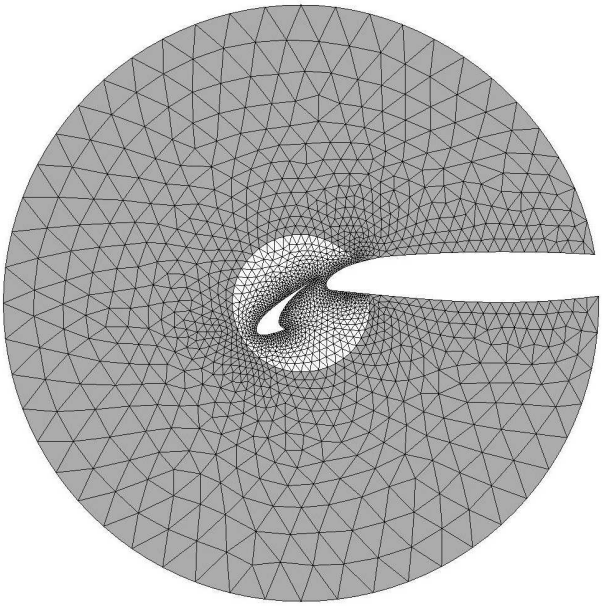

FIGURE 10. Finite element grid of slat cove with annular PML (shaded region).

high lift configuration Hein *et al.* (2005) showed that these low-frequency resonances agree fairly well with the measured low-frequency tones of Pott-Pollenske *et al.* (2003) even though their flap extended only over half the span and therefore three-dimensional effects might be expected. For higher frequencies the highly damped slat cove resonances of figure 11 determine the peaks in the spectrum which we marked by arrows in figure 12. It is interesting to note that even the peak tone in the experiment of Pott-Pollenske *et al.* (2003) seems to be near the first slat cove resonance marked by (a) in figure 12. The eigenfunctions corresponding to the first five marked peaks $(a), \ldots, (e)$ are shown in figure 13. In the cove region the eigenfunctions (c), (d) and (e) of figure 13 agree quite well with the three slat cove eigenfunctions depicted in figure 11. Near $Re(K/2\pi) = 13$ the two resonance branches seem to interchange similar to the x-symmetric and x-antisymmetric resonances in figure 5b, but it is not clear what that means physically.

5. Variation of resonances with slat cove parameter changes

The traditional geometric parameters determining the aerodynamic performance of leading edge slats are the slat angle δ_s, the slat overlap o_s and the slat gap g_s as sketched in figure 14. Following Pott-Pollenske *et al.* (2003) we used in our baseline configuration of the previous section the slat cove parameters $\delta_s = 26^o$, $o_s = -0.018$, and $g_s = 0.0217$. Hein *et al.* (2005) varied these parameters for the generic three-element high lift configuration of Pott-Pollenske *et al.* (2003) and found only negligible changes for the low-frequency resonances up to $Re(K/2\pi) = 5$. In the following we investigate the influence of the slat cove parameters on the high-frequency resonances by extending the frequency range by a factor of four up to $Re(K/2\pi) = 20$.

First we vary the slat angle δ_s keeping the slat overlap $o_s = -0.018$ and slat gap $g_s = 0.0217$ fixed. The results for $\delta_s = 10^o, 20^o$ and 30^o are shown in figure 15 complementing figure 12 with $\delta_s = 26^o$. We increased the polynomial order up to $p = 14$ and $p = 16$ to check the convergence of the resonances shown and eliminate spurious modes. However,

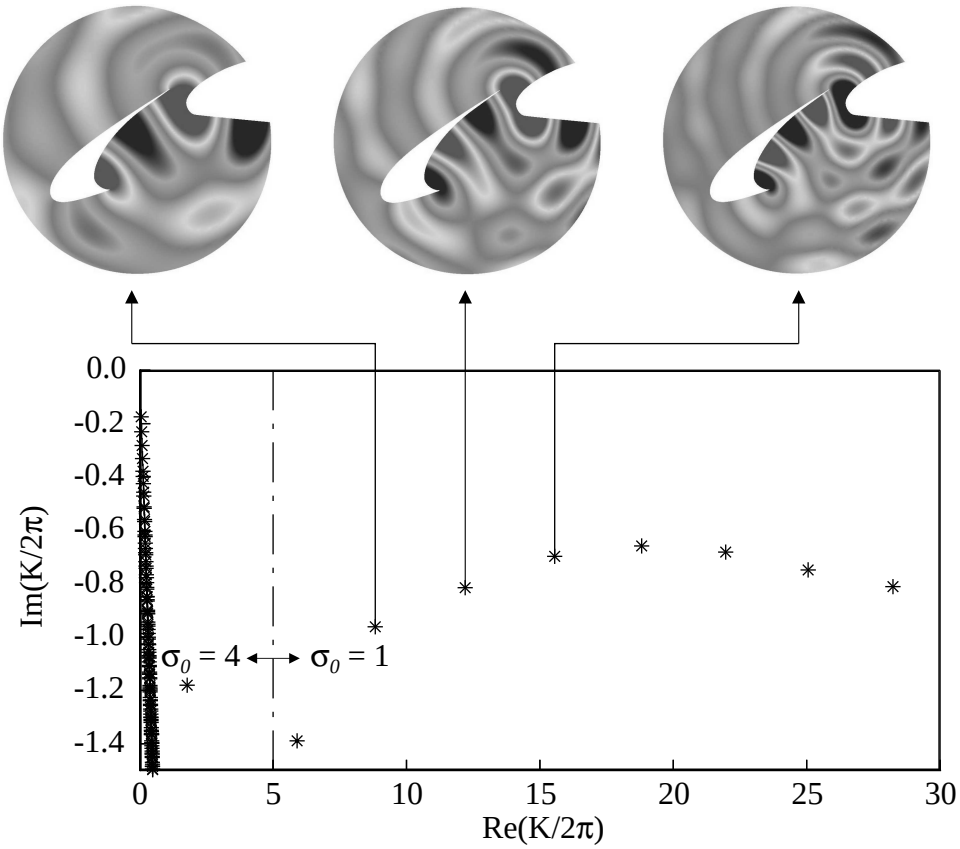

FIGURE 11. Slat cove resonances (∗) for high lift configuration with slat angle $\delta_s = 26^o$, slat overlap $o_s = 0.018$, slat gap $g_s = 0.0217$ and annular PML: $d_{PML} = 0.5$, $\sigma_0 = 1$, $\Delta = 0.08$ and $p = 12$. The two overlaping spectra are patched together at the dash-dotted line.

with $p = 16$ we reached the limits of our computational facilities. Again, the peaks in the spectrum are determined by the highly damped slat cove resonances marked by the asterisks. At lower δ_s, cf. figure 15a, the slat cove resonances have lower damping at the higher frequencies resulting in more distinct resonance peaks there. But in general the slat cove resonances do not change much by varying δ_s from 10^o to 30^o.

Next we vary the slat overlap o_s keeping the slat angle $\delta_s = 26^o$ and the slat gap $g_s = 0.0217$ fixed. The resulting spectra for negative and posive slat overlaps are shown in figure 16 complementing figure 12 with $o_s = -0.018$. With increasing (positive) overlap the slat cove resonances become more damped at higher frequencies smoothing the correponding resonant peaks. Slat overlap seems to have a large influence on the slat cove resonances.

Finally we vary the slat gap g_s keeping the slat angle $\delta_s = 26^o$ and the slat overlap $o_s = +0.005$ fixed. We selected the positive slat overlap $o_s = +0.005$ so that we could let the slat gap g_s go to zero and thereby obtain a closed cavity for comparison even though this case is of no interest for actual high lift configurations. The resulting spectra are shown in figure 17. For $g_s = 0$, cf. figure 17c, we see clearly how the slat cove resonances dominate at higher frequencies and the slat cove resonance at $Re(K/2\pi) \approx 17$ agrees almost exactly with the weakly damped resonance of the high lift system. From this we

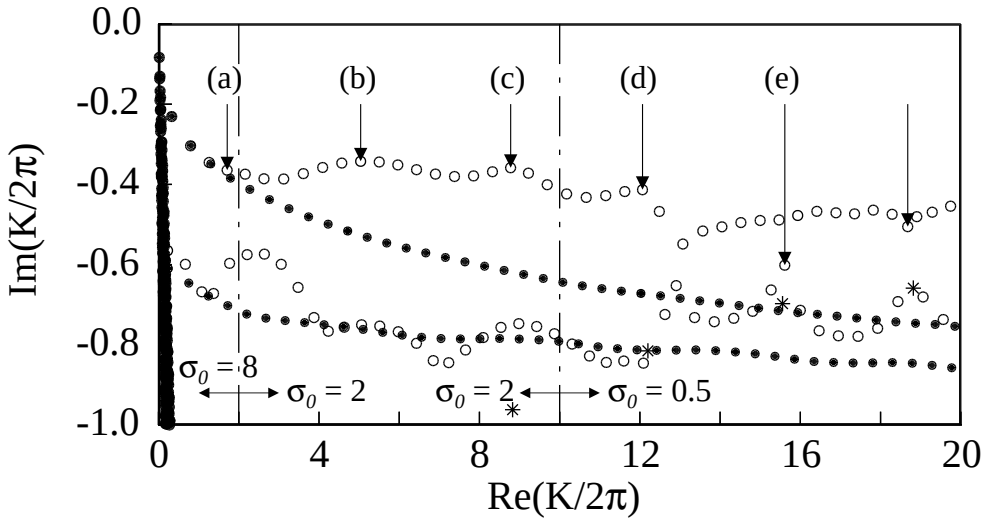

FIGURE 12. Resonances (○) for high lift configuration with slat angle $\delta_s = 26^o$, slat overlap $o_s = -0.018$, slat gap $g_s = 0.0217$ and rectangular PML: $d_{PML} = 0.5$, $\Delta = 0.15$ and $p = 12$. Also included are the surface wave resonances (•) of the clean wing of figure 8 and the slat cove resonances (∗) of figure 11.

conclude that a cavity closed at the bottom has resonances with much lower damping than a cavity with an opening at the cavity bottom. A high lift system has such an opening between the trailing edge and the main wing and therefore shows higher damping than our model problem of Section 3. However, the effect of mean flow through such an opening still has to be assessed.

Summarising we can say that the low-frequency resonances are determined by the surface-wave resonances which are practically independent of slat cove geometry. The high-frequency peaks are determined by the longitudinal slat cove resonances which are highly dependent on the slat cove geometry in particular the slat overlap and slat gap but only to a lesser degree on the slat angle.

6. Conclusion

We computed acoustic resonances of a generic two-element high lift configuration with a single leading edge slat. These resonances are highly damped by radiation losses to infinity but could possibly be excited by unstable shear layers enhancing the response near those resonant frequencies. For the computation of the resonances we neglected mean flow effects assuming that mean flow is not important at the low Mach numbers of aircraft landing and approach. However, for the exciting shear-layer sources mean flow is essential. To avoid unphysical reflections at the truncated domain boundaries we employed perfectly matched layer boundary conditions in the form of the complex scaling method of atomic and molecular physics.

Introducing the simple model of a circular cylinder with a rectangular cutout we demonstrated the existence of two distinct types of resonance: the first type of resonance is due to surface waves and scales with the total circumference, i.e. the airfoil length. The second type of resonance corresponds to longitudinal resonances in a cavity, scales with the length of the cavity and dominates for our model problem. Similar types of resonance are found for the high lift system albeit the cavity resonances are much

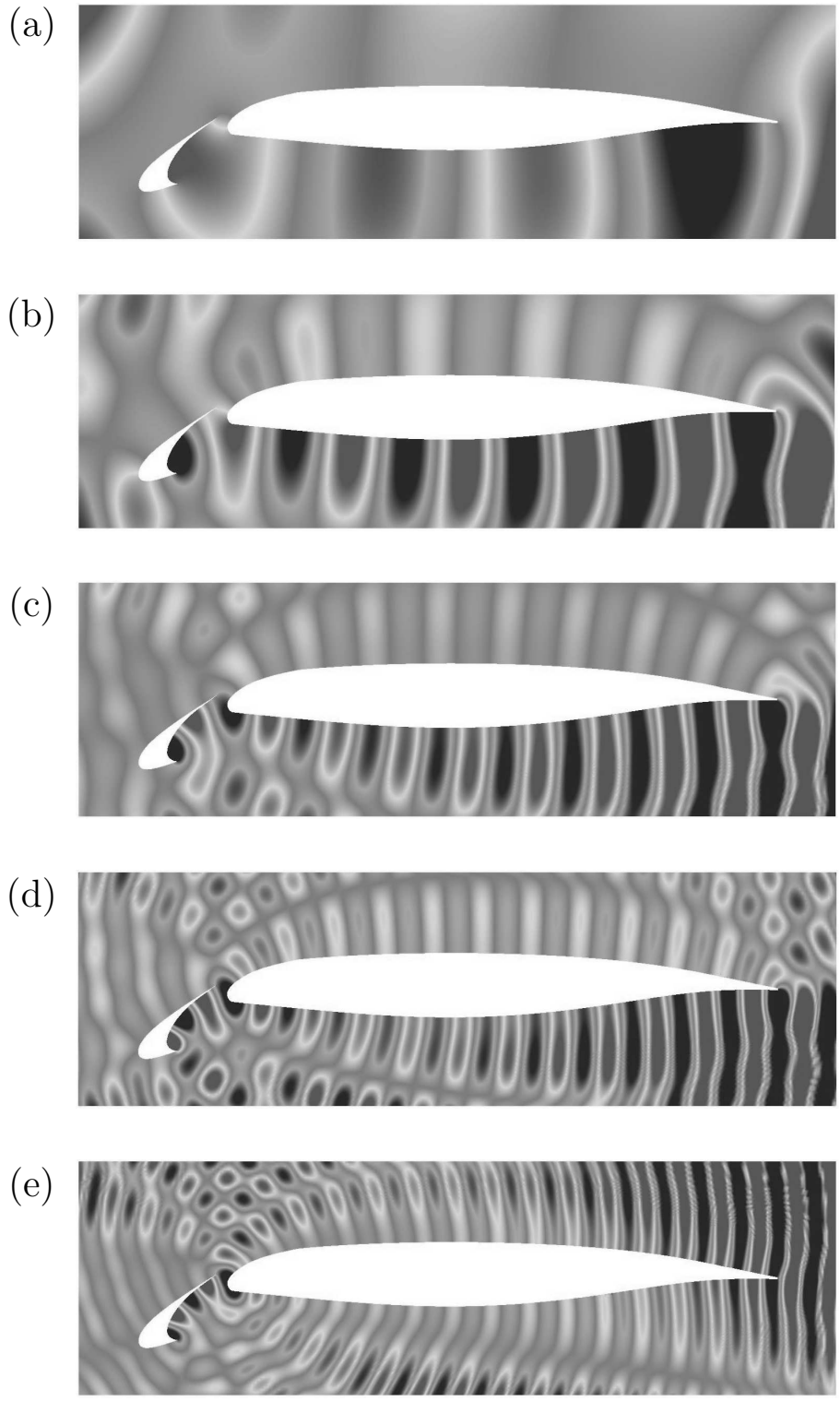

FIGURE 13. High lift configuration eigenfunctions $(a), \ldots, (e)$ corresponding to the five resonances marked in figure 12.

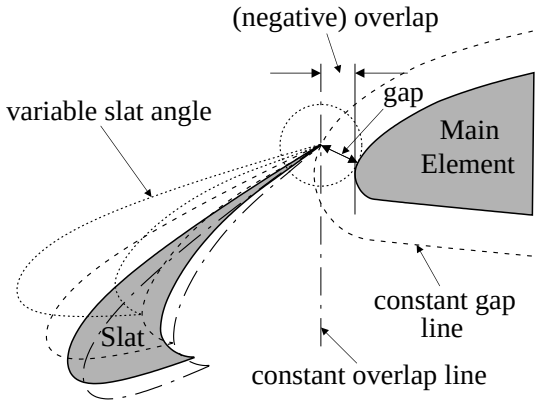

FIGURE 14. Slat cove parameters with $\delta_s = 10^o, 20^o, 26^o$ (shaded baseline configuration) and 30^o.

more damped due to the opening between the slat trailing edge and the main wing. Nevertheless, these longitudinal cavity resonances seem to determine the spectral peaks. Contrary to the transverse gap resonances of Tam & Pastouchenko (2001) and Agarwal & Morris (2002) between the slat trailing edge and the main wing our longitudinal cavity resonances are least damped near the frequencies of the longitudinal cavity resonances of the slat cove between the slat hook and the main wing. Varying the slat parameters we showed that the slat cove geometry, in particular the slat overlap and the slat gap, have a strong influence on the resonances and therefore on the response of the high lift system to shear-layer excitation. It is expected that the slat cove resonances also strongly influence the radiated noise pattern.

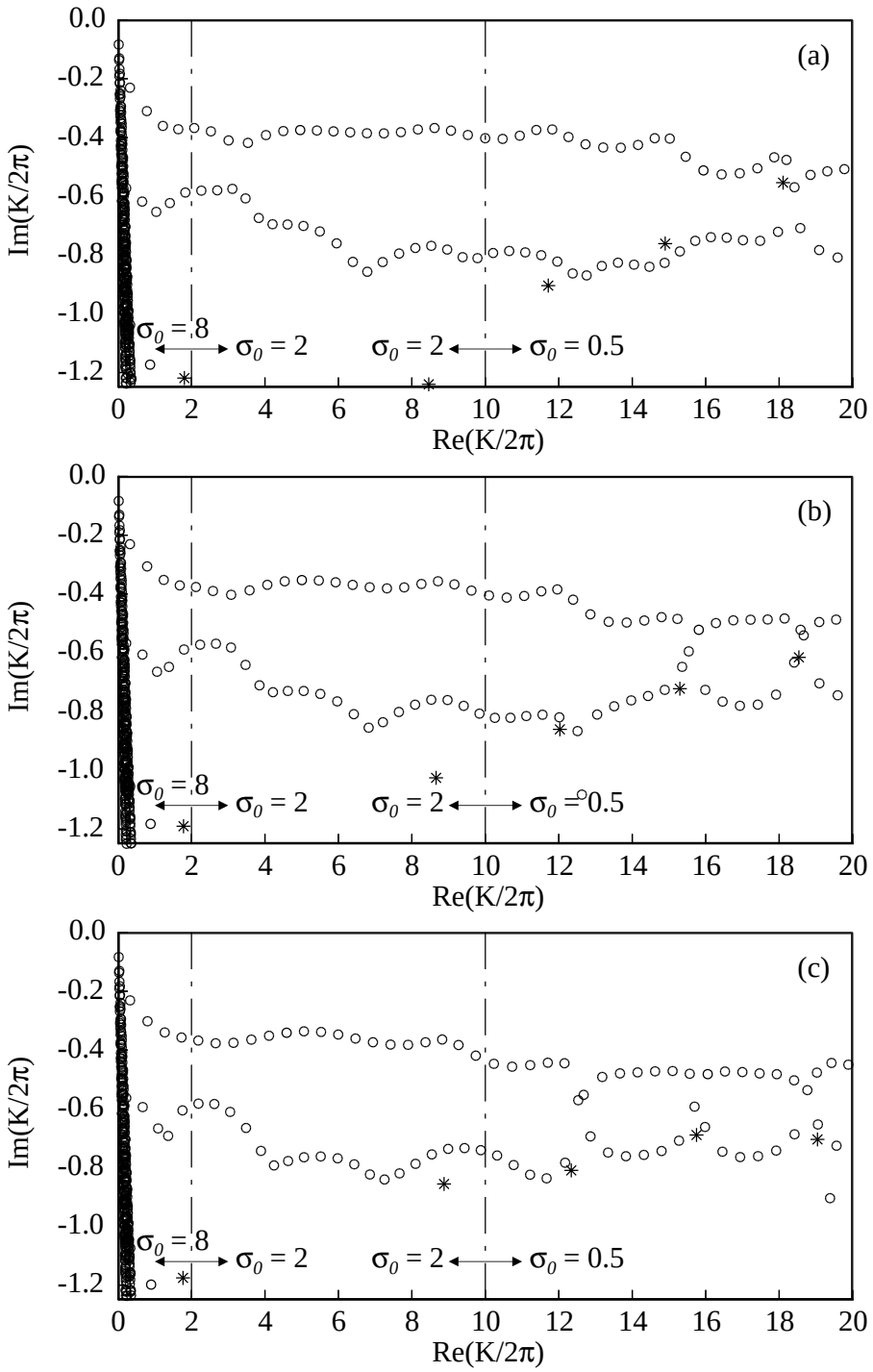

FIGURE 15. Influence of slat angle δ_s on resonances ($\circ$) of two-element high lift configuration with fixed slat overlap $o_s = -0.018$ and fixed slat gap $g_s = 0.0217$ using a rectangular PML: $d_{PML} = 0.5$, $\Delta = 0.15$ and $p = 16$. ($*$) denotes the slat cove resonances. (a) $\delta_s = 10^o$, (b) $\delta_s = 20^o$, (c) $\delta_s = 30^o$.

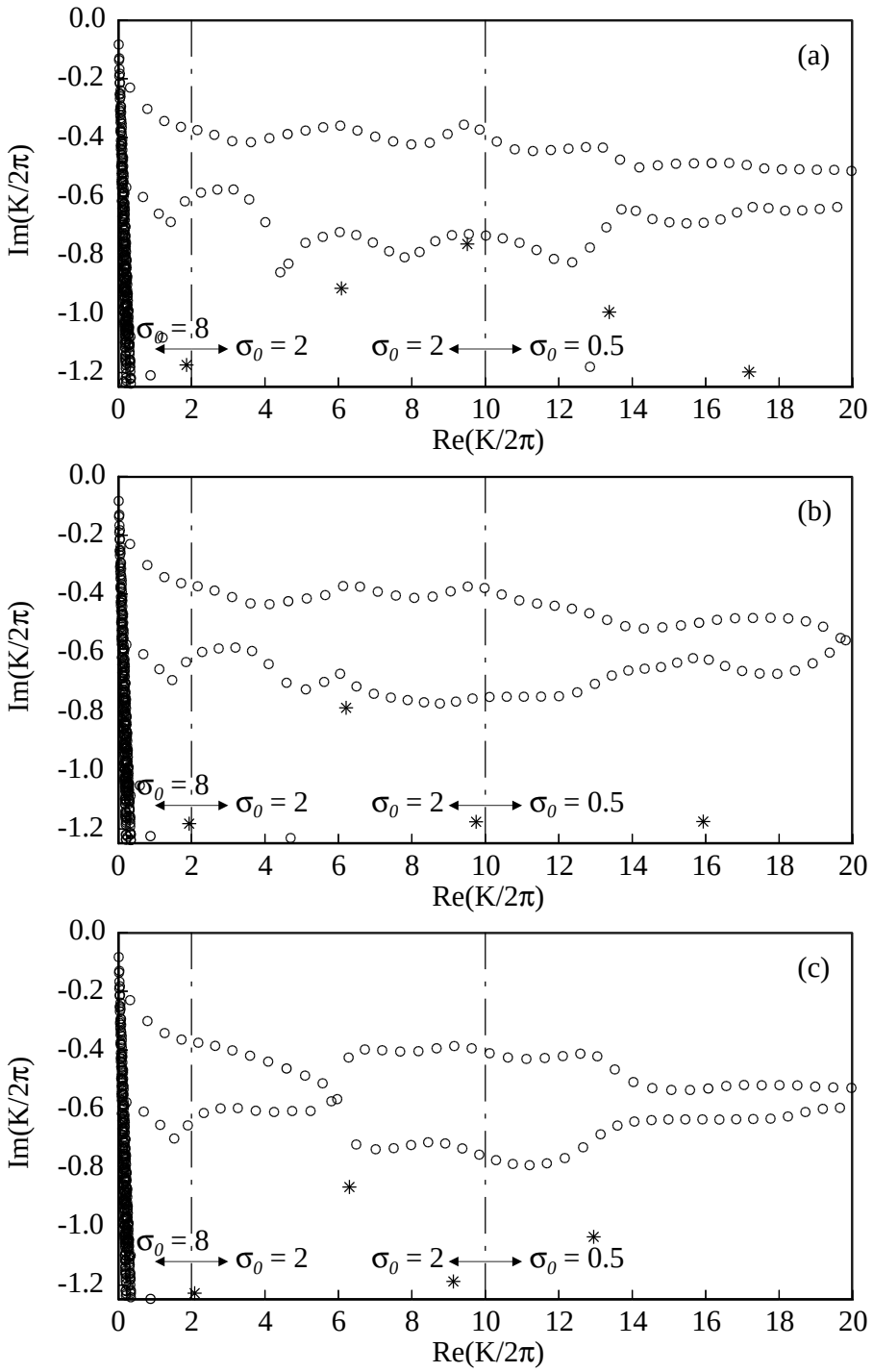

FIGURE 16. Influence of slat overlap o_s on resonances ($\circ$) of two-element high lift configuration with fixed slat angle $\delta_s = 26^o$ and fixed slat gap $g_s = 0.0217$ using a rectangular PML: $d_{PML} = 0.5$, $\Delta = 0.15$ and $p = 16$. ($*$) denotes the slat cove resonances. (a) $o_s = -0.005$, (b) $o_s = +0.005$, (c) $o_s = +0.02$.

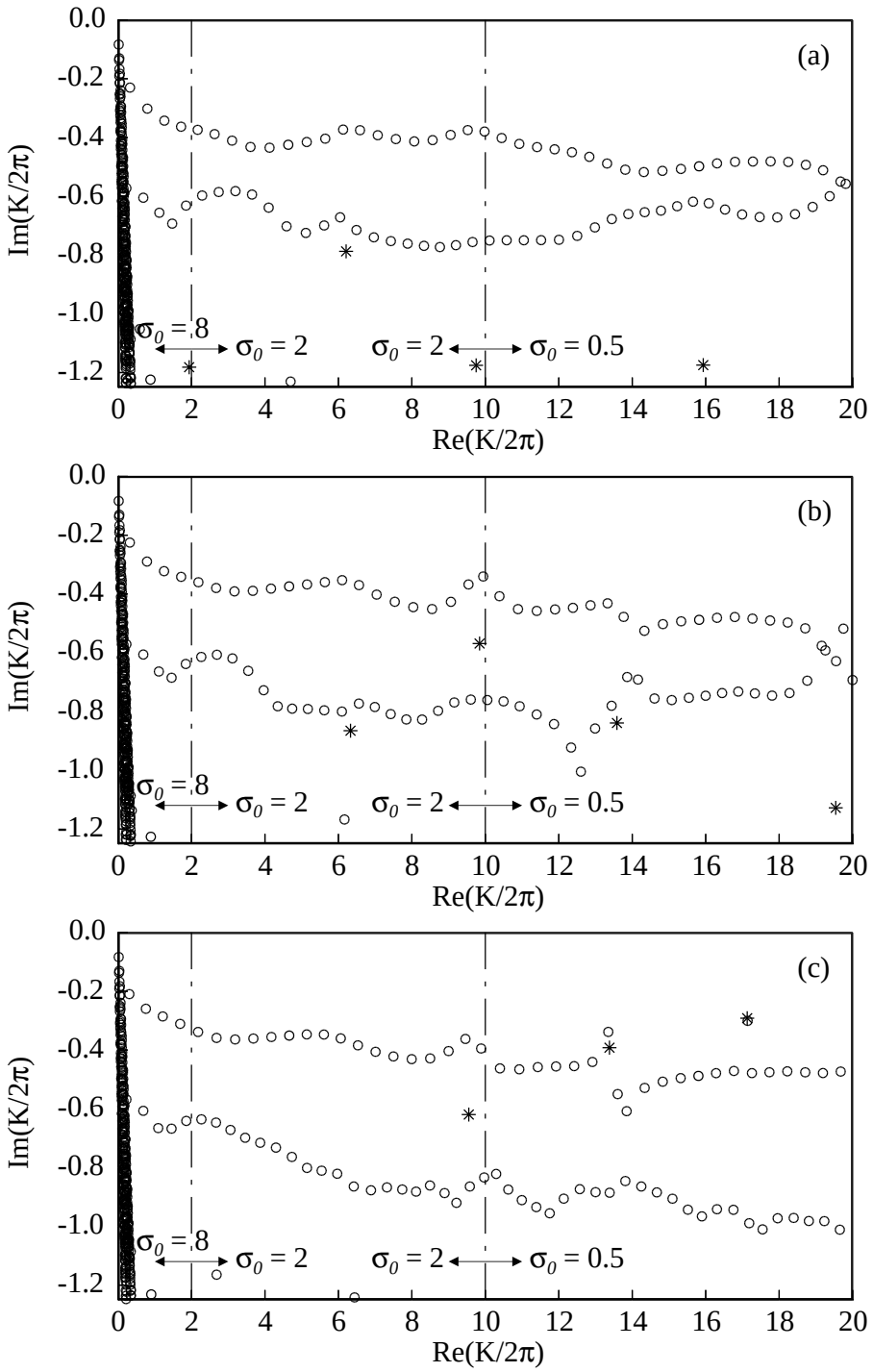

FIGURE 17. Influence of slat gap g_s on resonances ($\circ$) of two-element high lift configuration with fixed slat angle $\delta_s = 26^o$ and fixed slat overlap $o_s = +0.005$ using a rectangular PML: $d_{PML} = 0.5$, $\Delta = 0.15$ and $p = 16$. ($*$) denotes the slat cove resonances. (a) $g_s = 0.0217$, (b) $g_s = 0.01$, (c) $g_s = 0$.

References

AGARWAL, A. & MORRIS, P. 2002 Investigation of the physical mechanisms of tonal sound generation by slats. AIAA–Paper 2002–2575. 8th AIAA/CEAS Aeroacoustics Conference and Exhibit, Breckenridge, Colorado.

BÉRENGER, J. 1994 A perfectly matched layer for the absorption of electromagnetic waves. *J.Comput.Phys.* **114**, 185–200.

CHEW, W., JIN, J. & MICHIELSSEN, E. 1997 Complex coordinate stretching as a generalized absorbing boundary condition. *Microwave Optical Technol.Lett.* **15** (3), 144–147.

CHEW, W. & WEEDON, W. 1994 A 3-D perfectly matched medium from modified Maxwell's equation with stretched coordinates. *Microwave Optical Technol.Lett.* **7** (13), 599–604.

CHOUDHARI, M. & KHORRAMI, M. 2006 Slat cove unsteadiness: Effect of 3d flow structure. AIAA–Paper 2006–0211. 44th AIAA Aerospace Science Meeting and Exhibit, Reno, Nevada.

COLLINO, F. & MONK, P. 1998 The perfectly matched layer in curvilinear coordinates. *SIAM J.Sci.Comput.* **19** (6), 2061–2090.

CRIGHTON, D. 1991 Airframe noise. In *Aeroacoustics of Flight Vehicles: Theory and Practice. Vol.1: Noise Sources* (ed. H.H.Hubbard), pp. 391–447. NASA.

DAVY, R., MOENS, F. & REMY, H. 2002 Aeroacoustic behaviour of a 1/11 scale airbus model in the open anechoic wind tunnel CEPRA 19. AIAA–Paper 2002–2412. 8th AIAA/CEAS Aeroacoustics Conference and Exhibit, Breckenridge, Colorado.

DOBRZYNSKI, W., GEHLHAR, B. & BUCHHOLZ, H. 2001 Model and full scale high-lift wing wind tunnel experiments dedicated to airframe noise reduction. *Aerosp.Sci.Technol.* **5**, 27–33.

DOBRZYNSKI, W., NAGAKURA, K., GEHLHAR, B. & BUSCHBAUM, A. 1998 Airframe noise studies on wings with deployed high-lift devices. AIAA–Paper 98–2337. 4th AIAA/CEAS Aeroacoustics Conference, Toulouse, France.

DOBRZYNSKI, W. & POTT-POLLENSKE, M. 2001 Slat noise source studies for farfield noise prediction. AIAA–Paper 2001–2158. 7th AIAA/CEAS Aeroacoustics Conference, Maastricht, The Netherlands.

GROSCHE, F.-R., SCHNEIDER, G. & STIEWITT, H. 1997 Wind tunnel experiments on airframe noise sources of transport aircraft. AIAA–Paper 97–1642. 3rd AIAA/CEAS Aeroacoustics Conference, Atlanta, GA.

GUO, Y. 1997 A model for slat noise generation. AIAA–Paper 97–1647. 3rd AIAA/CEAS Aeroacoustics Conference, Atlanta, Georgia.

HAYES, J., HORNE, W., SODERMAN, P. & BENT, P. 1997 Airframe noise characteristics of a 4.7% scale DC-10 model. AIAA–Paper 97–1594. 3rd AIAA/CEAS Aeroacoustics Conference, Atlanta, Georgia.

HEIN, S., HOHAGE, T. & KOCH, W. 2004 On resonances in open systems. *J.Fluid Mech.* **506**, 255–284.

HEIN, S., KOCH, W. & SCHÖBERL, J. 2005 Acoustic resonances in a 2d high lift configuration and a 3d open cavity. AIAA–Paper 2005–2867. 11th AIAA/CEAS Aeroacoustics Conference, Monterey, California.

HELMHOLTZ, H. 1954 *On the Sensations of Tone*, 2nd edn. New York: Dover.

HEYMAN, E. & FELSEN, L. 1983 Creeping waves and resonances in transient scattering by smooth convex objects. *IEEE Trans.Antennas Propagat.* **31** (3), 426–437.

HISLOP, P. & SIGAL, I. 1996 *Introduction to Spectral Theory*. Springer.

HOHAGE, T., SCHMIDT, F. & ZSCHIEDRICH, L. 2003*a* Solving time-harmonic scattering problems based on the pole condition. I: Theory. *SIAM J. Math. Anal.* **35**, 183–210.

Hohage, T., Schmidt, F. & Zschiedrich, L. 2003*b* Solving time-harmonic scattering problems based on the pole condition. II: Convergence of the PML method. *SIAM J. Math. Anal.* **35**, 547–560.

Horne, W., James, K., Arledge, T., Soderman, P., Burnside, N. & Jaeger, S. 2005 Measurements of 26%-scale 777 airframe noise in the NASA Ames 40- by 80 foot wind tunnel. AIAA–Paper 2005–2810. 11th AIAA/CEAS Aeroacoustics Conference, Monterey, California.

Hu, F. 2004 Absorbing boundary conditions. *I.J.Comput.Fluid Dyn.* **18** (6), 513–522.

Jenkins, L., Khorrami, M. & Choudhari, M. 2004 Characterization of unsteady flow structures near leading-edge slat: Part I. PIV measurements. AIAA–Paper 2004–2801. 10th AIAA/CEAS Aeroacoustics Conference, Manchester, UK.

Kaepernick, K., Koop, L. & Ehrenfried, K. 2005 Investigation of the unsteady flow field inside a leading edge slat cove. AIAA–Paper 2005–2813. 11th AIAA/CEAS Aeroacoustics Conference, Monterey, California.

Khorrami, M., Berkman, M. & Choudhari, M. 2000 Unsteady flow computations of a slat with a blunt trailing edge. *AIAA Journal* **38**, 2050–2058.

Khorrami, M., Choudhari, M. & Jenkins, L. 2004 Characterization of unsteady flow structures near leading-edge slat: Part II. 2d computations. AIAA–Paper 2004–2802. 10th AIAA/CEAS Aeroacoustics Conference, Manchester, UK.

Khorrami, M., Singer, B. & Berkman, M. 2002 Time-accurate simulations and acoustic analysis of slat free shear layer. *AIAA Journal* **40**, 1284–1291.

Koch, W. 2005 Acoustic resonances in rectangular open cavities. *AIAA Journal* **43** (11), 2342–2349.

Lassas, M. & Somersalo, E. 1998 On the existence and convergence of the solution of PML equations. *Computing* **60** (3), 229–241.

Lax, P. & Phillips, R. 1967 *Scattering theory*. New York: Academic Press.

Michel, U., Barsikow, B., Helbig, J., Hellmig, M. & Schüttepelz, M. 1998 Flyover noise measurements on landing aircraft with a microphone array. AIAA–Paper 98–2336. 4th AIAA/CEAS Aeroacoustics Conference, Toulouse, France.

Moiseyev, N. 1998 Quantum theory of resonances: calculating energies, widths and cross-sections by complex scaling. *Physics Reports* **302**, 211–293.

Morse, P. & Ingard, K. 1968 *Theoretical Acoustics*. McGraw-Hill.

Oerlemans, S. & Sijtsma, P. 2004 Acoustic array measurements of a 1:10.6 scaled airbus A340 model. AIAA–Paper 2004–2924. 10th AIAA/CEAS Aeroacoustics Conference, Manchester, UK.

Olson, S., Thomas, F. & Nelson, R. 2000 A preliminary investigation into slat noise production mechanisms in high-lift configuration. AIAA–Paper 2000–4508. 18th AIAA Applied Aerodynamics Conference, Denver, CO.

Olson, S., Thomas, F. & Nelson, R. 2001 Mechanisms of slat noise production in a 2D multi-element airfoil configuration. AIAA–Paper 2001–2156. 7th AIAA/CEAS Aeroacoustics Conference, Maastricht, The Netherlands.

Piet, J., Michel, U. & Böhning, P. 2002 Localization of the acoustic sources of the A340 with a large phased microphone array during flight tests. AIAA–Paper 2002–2506. 8th AIAA/CEAS Aeroacoustics Conference and Exhibit, Breckenridge, Colorado.

Pott-Pollenske, M., Alvarez-Gonzalez, J. & Dobrzynski, W. 2003 Effect of slat gap on farfield noise and correlation with local flow characteristics. AIAA–Paper 2003–3228. 9th AIAA/CEAS Aeroacoustics Conference, Hilton Head, South Carolina.

Reed, M. & Simon, B. 1978 *Methods of Modern Mathematical Physics IV*. New York: Academic Press.

ROGER, M. & PÈRENNÉS, S. 2000 Low-frequency noise sources in two-dimensional high-lift devices. AIAA–Paper 2000–1972. 6th AIAA/CEAS Aeroacoustics Conference, Lahaina, Hawaii.

SCHÖBERL, J. 1997 NETGEN An advancing front 2D/3D-mesh generator based on abstract rules. *Computing and Visualization in Science* **1**, 41–52.

SINGER, B., LOCKARD, D. & BRENTNER, K. 2000 Computational aeroacoustic analysis of slat trailing-edge flow. *AIAA Journal* **38**, 1558–1564.

SODERMAN, P., KAFYEKE, F., BURNSIDE, N., CHANDRASEKHARAN, R., JAEGER, S. & BOUDREAU, J. 2002 Aerodynamic noise induced by laminar and turbulent boundary layers over rectangular cavities. AIAA–Paper 2002–2406. 8th AIAA/CEAS Aeroacoustics Conference and Exhibit, Breckenridge, Colorado.

STOKER, R., GUO, Y., STREET, C. & BURNSIDE, N. 2003 Airframe noise source locations of a 777 aircraft in flight and comparisons with past model scale tests. AIAA–Paper 2003–3232. 9th AIAA/CEAS Aeroacoustics Conference, Hilton Head, South Carolina.

TAKEDA, K., ASHCROFT, G., ZHANG, X. & NELSON, P. 2001 Unsteady aerodynamics of slat cove flow in a high-lift device configuration. AIAA–Paper 2001–0706. 39th AIAA Aerospace Sciences Meeting and Exhibit, Reno, Nevada.

TAKEDA, K., ZHANG, X. & NELSON, P. 2002 Unsteady aerodynamics and aeroacoustics of a high-lift device configuration. AIAA–Paper 2002–0570. 40th AIAA Aerospace Sciences Meeting and Exhibit, Reno, NV.

TAKEDA, K., ZHANG, X. & NELSON, P. 2004 Computational aeroacoustic simulations of leading-edge slat flow. *J.Sound Vibration* **270**, 559–572.

TAM, C. 1976 The acoustic modes of a two-dimensional rectangular cavity. *J.Sound Vibration* **49** (3), 353–364.

TAM, C. & PASTOUCHENKO, N. 2001 Gap tones. *AIAA Journal* **39**, 1442–1448.

ÜBERALL, H., DRAGONETTE, L. & FLAX, L. 1977 Relation between creeping waves and normal modes of vibration of a curved body. *J.Acoust.Soc.Amer.* **61**, 711–715.

ZWORSKI, M. 1999 Resonances in physics and geometry. *Notices of the AMS* **319**, 319–328.

Institut für Numerische und Angewandte Mathematik
Universität Göttingen
Lotzestr. 16-18
D - 37083 Göttingen

Telefon: 0551/394512
Telefax: 0551/393944

Email: trapp@math.uni-goettingen.de URL: http://www.num.math.uni-goettingen.de

Verzeichnis der erschienenen Preprints:

2006-01	R. Schaback	Limit Problems for Interpolation by Analytic Radial Basis Function
2006-02	N. Bissantz, T. Hohage, A. Munk, F. Ruymgaart	Convergence rates of general regularization methods for statistical inverse problems and applications
2006-03	J. Brimberg, H. Juel, A. Schöbel	Locating a circle on a sphere
2006-04	J. Brimberg, H. Juel, A. Schöbel	Locating a circle on the plane using the minimax criterion
2006-05	L. Ling, R. Opfer, R. Schaback	Results on Meshless Collocation Techniques
2006-06	G. Lube, T. Knopp et.al.	Domain decomposition methods for indoor air flow simulation
2006-07	T. Apel, T. Knopp, G. Lube	Stabilized finite element methods with anisotropic mesh refinement for the Oseen problem
2006-08	R. Schaback	Recovery of Functions From Weak Data Using Unsymmetric Meshless Kernel-Based Methods
2006-09	H.W. Hannacher, S. Horn, A. Schbel	Stop Location Design in Public Transportation Networks: Covering and Accessibility Objective
2006-10	Q.T. Le Gia, F.J. Narcowich, J.D. Ward, H. Wendland	Continuous and Discrete Least-Squares Approximation by Radial Basis Functions on Spheres
2006-11	R. Schaback	Unsymmetric Meshless Methods for Operator Equations
2006-12	P. Giesl, H. Wendland	Meshless Collocation: Error Estimates with Application to Dynamical Systems
2006-13	H. Wendland	On the stability of meshless symmetric collocation for boundary value problems
2006-14	G. Lube	Stabilized FEM for incompressible flow. Critical review and new trends
2006-15	J. Puerto, A. Schöbel, S. Schwarze	A Class of Infinite Potential Games
2006-16	S. Hein, T. Hohage, W. Koch, J. Schöberl	Acoustic Resonances in High Lift Configuration